



# Simulation of Ferrochrome Settling Behavior in a Submerged Arc Furnace Using a Multiphysics and Multiphase Model

YANG YU, BAOKUAN LI, ZHONGQIU LIU, FENGSHENG QI, CHENGJUN LIU, WENJIE RONG, and SHIBO KUANG

The ferrochrome settling behavior significantly affects the smelting performance of a submerged arc furnace. This paper presents a three-dimensional (3D) transient mathematical model simulating the complex multiphase flow and thermochemical phenomena inside an industrial furnace. *Via* the model, the smelting phenomena are clarified in terms of electromagnetic field, temperature distribution, multiphase flows, and ferrochrome productivity. The effects of phase voltage varying from 75 to 85 V are quantified as well. Furthermore, the interface among the furnace burden, slag, and ferrochrome is used to characterize the ferrochrome settling behavior. The results show that the real-time reduction reactions determine the location and output of ferrochrome droplets. As the phase voltage increases, the current increases by 13.06 pct, the ratio of voltage drop between the furnace burden and submerged arc increases by 0.17 pct. The path of ferrochrome droplets affects the high temperature zone, which is the largest at a phase voltage of 85 V. At this phase voltage, the droplet velocity is the highest and the ferrochrome output is 6.86 t/h. Correspondingly, the energy consumption is 3363.81 kWh/t and the content of Cr is 57.09 pct. The results in the present study can be employed for decision-making on improving the operation of submerged arc furnaces to reduce the energy consumption and improve ferrochrome quality.

<https://doi.org/10.1007/s11663-023-02817-1>

© The Minerals, Metals & Materials Society and ASM International 2023

## I. INTRODUCTION

FERROCHROME plays a significant role in steel-making due to its ability to improve steel quality.<sup>[1]</sup> Ferrochrome smelting, as a huge energy consumption technology, usually needs tremendous electric energy in the form of alternating current (AC) or direct current (DC).<sup>[2]</sup> There are two common ferrochrome smelting systems, *i.e.*, the rotary kiln-electric furnace system

(RKEF) and the sintering-preheating-submerged arc furnace system (SPSF).<sup>[3]</sup> In either system, submerged arc furnaces (SAF) plays a vital role in ferrochrome production.<sup>[4]</sup> SAF is an energy-intensive reactor for producing ferronickel, ferromanganese, ferrochrome, and other ferroalloys.

SAF structure and the associated smelting phenomena are illustrated schematically in Figure 1. A typical SAF is mainly composed of a furnace lining, three self-baked electrodes, a power supply equipment, a control system, a feeding system, and a water-cooling system.<sup>[5]</sup> The smelting process contains arc forming stage, furnace burden heating stage, stable smelting stage, and tapping stage.<sup>[6,7]</sup> In the SAF, the smelting process runs for days to reach the stable smelting stage. During operations, some transient phenomena exist, including electro-thermal conversion, heat and mass transfer, and multiphase interactions. The furnace burden is melted by the intense heat generated by the arc heat and Joule heat.<sup>[8,9]</sup> The local intense heat lifts the furnace temperature, eventually activates the reduction reactions of furnace burden, and generates the slag and ferrochrome. The molten slag and alloy drop to the bottom of the furnace.

---

YANG YU, BAOKUAN LI, ZHONGQIU LIU, FENGSHENG QI, CHENGJUN LIU, and WENJIE RONG are with the College of Metallurgy, Northeastern University, Shenyang 110819, Liaoning, P.R. China and with the National Frontiers Science Center for Industrial Intelligence and Systems Optimization, Northeastern University, Shenyang 110819, Liaoning, P.R. China and also with the Key Laboratory of Data Analytics and Optimization for Smart Industry (Northeastern University), Ministry of Education, Shenyang 110819, Liaoning, P.R. China. Contact e-mails: libk@smm.neu.edu.cn; liuzq@smm.neu.edu.cn SHIBO KUANG is with the Department of Chemical Engineering, ARC Research Hub for Computational Particle Technology, Monash University, Clayton, VIC 3800, Australia.

Manuscript submitted October 9, 2022; accepted May 3, 2023.

Article published online June 6, 2023.

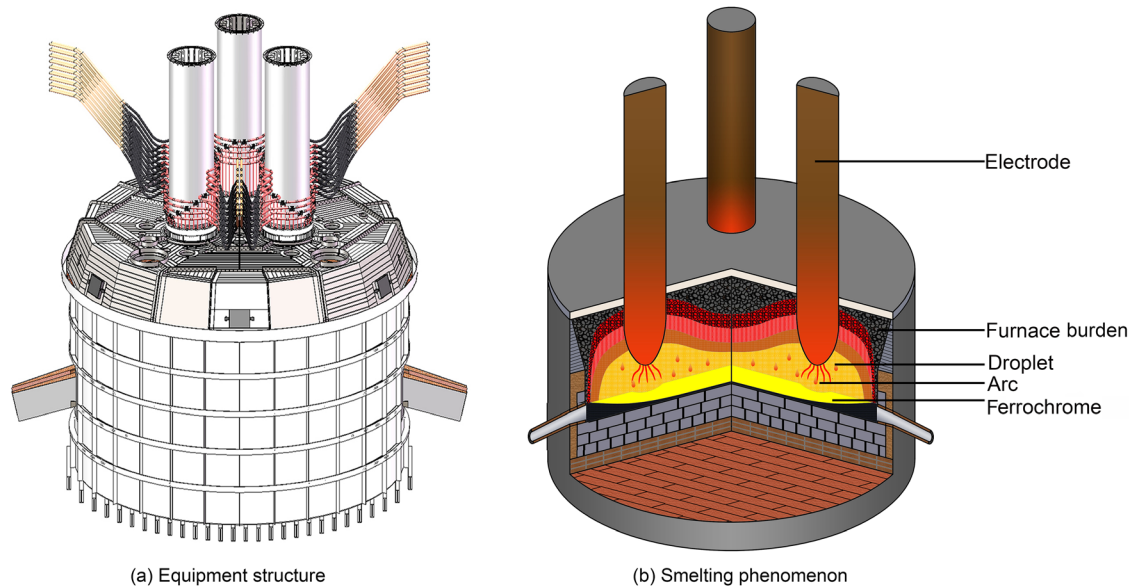


Fig. 1—Schematic illustration of smelting process in SAF: (a) Equipment structure. (b) Smelting phenomenon.

To remedy the measurement difficulties of current experimental studies, numerical modelling has become an essential tool for studying the smelting process in SAF.<sup>[10,11]</sup> The history of smelting simulation has experienced developments from the alternating current arc and direct current arc in the furnace,<sup>[8,12]</sup> industry operation control,<sup>[13–16]</sup> to metallurgical state, benefiting from the increased computer capacity and the improved knowledge of the furnace.<sup>[17–20]</sup> Despite the extensive research efforts, the above-discussed studies focused on the smelting process. Unfortunately, the prediction of ferroalloy productivity is neglected in the previous modeling framework.

To capture the transient smelting process, researchers have developed different SAF models. For instance, Andresen and Tuset<sup>[21]</sup> developed a 2D axisymmetric dynamic model, which incorporated the sub-models for direct current electric arc, fluid flow, and heterogeneous chemical reactions. It was used to describe the high temperature smelting process of the carbothermic silicon metal. Scheepers *et al.*<sup>[22,23]</sup> proposed a simplified furnace model describing the packed bed region with the reactions and heat transfer. The associated material properties were explicitly considered in the furnace materials phase. The stationary layer consisting of the slag and ferrophosphorus phases was neglected in the model. Wang *et al.*<sup>[24]</sup> established a 3D model considering the electromagnetic, thermal, and fluid flow fields to investigate the steady state in the process of MgO production. The shape of the molten bath was also considered, which was measured in situ during the furnace operation. Karalis *et al.*<sup>[25]</sup> simulated the ferromanganese heating process. A 2D model was presented, which included the equations of the electric potential, momentum and heat transfer in the fixed regions of the air, slag, ferromanganese, and firebricks. Bezuidenhout *et al.*<sup>[26]</sup> developed a two-phase model to capture the interactions between different fluid layers and carbon

monoxide released from the immersed electrode surface in the platinum group metal smelting. Kadkhodabeigi *et al.*<sup>[27]</sup> adopted a 3D two-phase flow model to capture the gas–liquid flow characteristics and their impact on the tapping process in a SAF for the silicon and ferrochrome. Xia *et al.*<sup>[28]</sup> studied the nickel droplet settling behavior in an electric furnace by simulation, but the droplet settling behavior was set according to the droplet volume fraction distribution and the droplet trajectories.

All these modeling efforts have provided good references for this study. However, the furnaces considered previously were mainly used to produce other ferroalloys instead of ferrochrome. Different ferroalloy production may represent somewhat different multiphysics and multiphase phenomena. More importantly, all the previous models were conducted given productivity under specified conditions. However, in practice, the productivity related to the droplet settling behavior depends on specific SAF conditions. In these circumstances, given productivity and SAF conditions in simulations may mismatch each other. Overcoming this problem necessitates the prediction of productivity under various conditions.

In the present study, a three-dimensional transient model is developed to describe the smelting process involving complex electro-thermal conversion, inter-phase mass transfer and thermo-chemical phenomena in a SAF at an industrial scale. The measured temperature and energy consumption are used to evaluate the accuracy of the model. Then, the results are analyzed in detail regarding the electromagnetic, temperature, flow, and reactant mass fraction fields. The performance of ferrochrome droplets is also investigated. The results improve understanding of the relationship between the electric input and smelting phenomena. Ultimately, they will help increase productivity and reduce the energy consumption of SAF.

## II. MODEL DESCRIPTION

The integrated model is developed to simulate the smelting phenomena at the stable smelting stage. Figure 2 shows the framework of the model, which describes the complex physical and chemical phenomena involving electro-thermal conversion, heat and mass transfer, and multiphase interaction. The modeling framework is accomplished by coupling four submodels for electromagnetic, heat transfer, reduction reactions, and multiphase flows. Details about the model are given below.

### A. Assumptions and Simplifications

To reduce the required computational resource for simulations at an industrial scale, several assumptions and simplifications are summarized as follows:

- The burden is evenly mixed in the furnace and fills the furnace. It is treated as a fluid region whose viscosity varies with temperature. The viscosity is infinitely large below the liquid temperature. It is consistent with that of molten ore above the liquid temperature.
- SAF is an electric furnace. The structure details of the electrode are not considered.
- The physical properties of the slag and ferrochrome are constant.
- To calculate the energy consumption, the power factor  $\cos\varphi$  and short network electric resistance  $R_{SN}$  are set to 0.86 and 0.149 m $\Omega$  according to the industry practice. The electrical conductivity of the electrode is 225000 S/m.<sup>[16]</sup>

### B. Mathematical Model

#### 1. Electromagnetic submodel

A transient electro-thermal conversion is modeled using Maxwell's equations, Ohm's law and arc characteristics to describe the electromagnetic distribution inside the SAF. The following equation is obtained as<sup>[15]</sup>:

$$\sigma \frac{\partial \vec{A}}{\partial t} - \nabla \cdot \left( \frac{1}{\mu_0} \nabla \vec{A} \right) = -\sigma \nabla \varphi \quad [1]$$

where  $\mu_0$  is the magnetic conductivity,  $\sigma$  is the electrical conductivity. The electric potential  $\varphi$  is expressed as:

$$\nabla^2 \varphi = 0 \quad [2]$$

Assuming the Coulomb condition gives by:

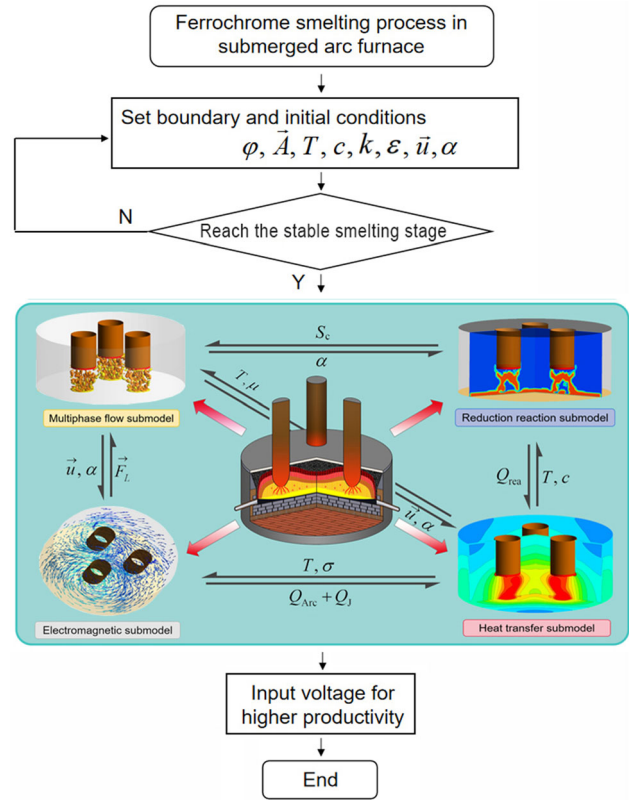


Fig. 2—Framework of the proposed model.

$$\nabla \cdot \vec{A} = 0 \quad [3]$$

where  $\vec{A}$  is the magnetic vector potential. The electric current density  $\vec{J}$  is described by:

$$\vec{J} = \sigma \left( -\nabla \varphi - \frac{\partial \vec{A}}{\partial t} \right) \quad [4]$$

The magnetic field  $\vec{B}$  and Lorentz force  $\vec{F}_L$  are computed by Eqs. [4] and [5], respectively:

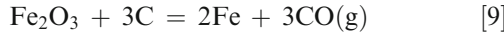
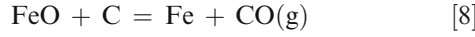
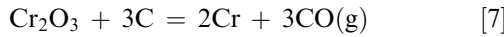
$$\vec{B} = \nabla \times \vec{A} \quad [5]$$

$$\vec{F}_L = \vec{J} \times \vec{B} \quad [6]$$

When the current passes through the furnace, electro-thermal conversion occurs. Two factors affect the submerged arc: the arc length and the arc voltage drop. At the industrial scale, the arc length is 0.1 m.<sup>[8]</sup> The voltage distribution determines the arc voltage drop. The electric conductivity of the furnace burden and submerged arc varies with temperature.

## 2. Reduction reaction submodel

The smelting process involves an exhaustive list of complex chemical reactions and various chemical species in the SAF. Due to the small proportions of other reactions, the ferrochrome generation depends on the reduction reactions.<sup>[3]</sup> The overall reduction reactions are divided into three reactions, which are given as:



When the reduction reaction occurs, the state of ore with coke is solid. The factors affecting the reaction rate are the temperature, the time, the particle size, the mass ratio of ore/coke, and the presence of flux promoting. Among these factors, temperature and time play a decisive role in the reaction.<sup>[14]</sup> The reduction reaction parameters are based on Reference 7.  $X$  is the mass fractional conversion rate.  $t$  is the physical time.  $K$  is the constant of the reaction rate, which is related to the activation energy and pre-exponential term through the Arrhenius equation:

$$K = A \exp(-E_a/RT) \quad [10]$$

where  $A$  is the pre-exponential term,  $E_a$  is the activation energy, and  $R$  is the ideal gas constant, 8.314 J/(mol·K).

When the furnace satisfies the reaction conditions, the reduction reactions generate the ferrochrome phase. Due to the furnace burden, slag and ferrochrome are treated as immiscible fluids. The reactions mainly occur in the furnace burden. The temperature of iron oxides and  $\text{Cr}_2\text{O}_3$  with Gibbs free energy  $\Delta G < 0$  is 1173 K and 1373 K, respectively. However, the temperature of ore melting is 1773 K. Thus, the diffusion term for the burden is not activated. In these circumstances, the diffusion term is not activated. Thus, the mass fraction equation of reactants is given by:

$$\frac{\partial(\rho_1 c_j)}{\partial t} + \nabla \cdot (\rho_1 \vec{u} c_j) = S_C \quad [11]$$

where  $\rho_1$  is the density of furnace burden,  $c$  is the mass fraction of reactant,  $j$  is the serial number of reduction reactions. When  $j = 1$ , the reactant is  $\text{Cr}_2\text{O}_3$ . When  $j = 2$ , the reactant is iron oxides.  $S_C$  is the source term of the reduction reaction, which is consistent with the amount of mass transfer.

$$S_C = - \sum_j^2 N X_j \alpha_1 \rho_1 \quad [12]$$

where  $N$  represents whether the reaction occurs. When the reaction occurs,  $N = 1$ . Otherwise  $N = 0$ . The reaction temperature is obtained by the HSC software.  $\alpha_1$  is the volume fraction of furnace burden.

## 3. Heat transfer submodel

The electric and thermal information of the submerged arc is pre-calculated at the stable smelting stage.<sup>[6]</sup> The equivalent treatment on the arc heat is carried out in the energy equation. The interfaces between the submerged arc and furnace burden are named arc sidewall and arc bottom. The determination of Joule heat requires the electric conductivity of the furnace burden. The resultant heat adsorption due to the endothermic reactions is also added to the energy equations *via* source terms. The governing equation of energy is given by:

$$\frac{\partial}{\partial t} (\rho c_p T) + \nabla \cdot (\vec{u} \rho c_p T) = \nabla \cdot [\lambda \nabla T] + S_Q \quad [13]$$

where  $\rho$  is the multiphase density,  $\rho = \sum \alpha_i \rho_i$ ,  $\lambda$  is the thermal conductivity. The latent heat of melting is equivalently converted to the specific heat capacity  $c_p$ , calculated by:

$$c_p = \begin{cases} c_{ps} & T \leq T_s \\ \frac{c_{ps} - c_{pl}}{2} + \frac{L}{T - T_s} & T_s \leq T \leq T_l \\ c_{pl} & T \geq T_l \end{cases} \quad [14]$$

where  $c_{ps}$  is the specific heat capacity of solid,  $c_{pl}$  is the specific heat capacity of liquid,  $L$  is the latent heat of melting,  $T_s$  is the starting temperature of phase change, and  $T_l$  is the end temperature of phase change.  $S_Q$  is the source term of energy given by:

$$S_Q = Q_{Arc} + Q_J + Q_{Rea} \quad [15]$$

where  $Q_{Arc}$  is the arc heat, expressed as:

$$Q_{Arc} = \frac{\vec{J} \cdot \vec{J}}{\sigma_{Arc}} + \frac{5 K_B}{2 e} \vec{J} \nabla T \quad [16]$$

where  $\sigma_{Arc}$  is the electrical conductivity of arc,  $K_B$  is Boltzmann's constant, and  $e$  is the electronic charge.  $Q_J$  is the Joule heat, given by:

$$Q_J = \frac{\vec{J} \cdot \vec{J}}{\sigma_{Fur}} \quad [17]$$

where  $\sigma_{Fur}$  is the electrical conductivity of the furnace, and  $Q_{Rea}$  is the heat of the reduction reaction, computed by:

$$Q_{Rea} = \sum_j \frac{q_j \Delta c_j \rho_1}{M_j \Delta t} \times 1000 \quad [18]$$

where  $q$  is the heat absorbed by reduction reactions,  $\Delta c$  is the variation of mass fraction,  $M$  is the molar mass of the reactant, and  $\Delta t$  is the simulation time step.

DO radiation method is adopted to solve the radiative heat transfer on the surface of the furnace hearth.<sup>[22,29]</sup> The radiative transfer equation for an absorbing, emitting, and scattering medium at the position  $\vec{r}$  in the direction  $\vec{s}$  is given by:



$$\frac{dI(\vec{r}, \vec{s})}{ds} + (a + \sigma_s)I(\vec{r}, \vec{s}) = a(n')^2 \frac{\delta T^4}{4\pi} \int_0^{4\pi} I(\vec{r}, \vec{s}') \Phi(\vec{s}, \vec{s}') d\Omega' \quad [19]$$

where  $\vec{r}$  is the position vector,  $\vec{s}$  is the direction vector,  $\vec{s}'$  is the scattering direction vector,  $s$  is the path length,  $a$  is the absorption coefficient,  $n'$  is the refractive index,  $\sigma_s$  is the scattering coefficient,  $\delta$  is the Stefan-Boltzmann constant,  $5.669 \times 10^{-8} \text{ W}/(\text{m}^2 \cdot \text{K}^4)$ ,  $I$  is the radiation intensity which depends on the position ( $\vec{r}$ ) and the direction ( $\vec{s}$ ),  $\Phi$  is the phase function,  $\Omega'$  is the solid angle, and  $(a + \sigma_s)s$  is the optical thickness or opacity of the medium. Both scattering and absorption coefficients are set to 0.6.<sup>[24]</sup>

#### 4. Multiphase flow submodel

The accumulation of ore particles forms the furnace burden. The gap between the particles is filled by furnace gas. The furnace gas and particles constitute the furnace burden phase. The slag and ferrochrome are immiscible fluids. Because of the different densities, stratification occurs in the smelting process. Table I lists the compositions of all phases. The volume of fluid (VOF) model is adopted to explicitly track the interfaces of furnace burden, slag, and ferrochrome. The ferrochrome phase generates and settles into the furnace bottom when the reduction reactions occur. The equation of volume fraction is expressed as:

$$\frac{\partial(\alpha_i \rho_i)}{\partial t} + \nabla \cdot (\alpha_i \rho_i \vec{u}) = S_{i,j} \quad [20]$$

where  $\sum_{i=1}^m \alpha_i = 1$ ,  $i$  is the serial number of phase. By definition,  $i=1$  represents the furnace burden phase;  $i=2$  corresponds to the slag phase; and,  $i=3$  is the ferrochrome phase.  $S_{i,j}$  is the source term of mass transfer. When the furnace burden transfers mass to ferrochrome, the source term is defined as

$$S_{1-3,j} = \sum \frac{\rho_1 \alpha_1 N X_j M_P}{M_R} \quad [21]$$

where  $M_P$  is the molar mass of the product and  $M_R$  is the molar mass of the reactant. After the reaction, the remaining nonmetallic mineral materials enter the slag layer. The slag is tapping with the ferrochrome. The relationship of mass flow between the slag and ferrochrome can be established through industrial measurement. When the furnace burden transfers mass to slag,  $S_{i,j}$  is defined as:

$$S_{1-2,j} = p \times S_{1-3,j} \quad [22]$$

where  $p$  is the mass ratio of slag to ferrochrome. According to the Reference 34, the mass ratio of slag to ferrochrome is 1.3. The momentum exchange between furnace burden-slag-ferrochrome phase is driven by surface tension, Lorentz force, and gravity.

$$\frac{\partial(\rho \vec{u})}{\partial t} + \nabla \cdot (\rho \vec{u} \vec{u}) = -\nabla p + \nabla \cdot (\mu_{eff} \nabla \vec{u}) + \vec{F}_{st} + \vec{F}_L + \rho \vec{g} \quad [23]$$

where  $\vec{F}_{st}$  is the surface tension.  $\mu_{eff}$  is the effective viscosity composed of the turbulence viscosity,<sup>[23]</sup>  $\mu_{eff} = \mu_l + \mu_t$ .  $\mu_l$  and  $\mu_t$  are the laminar and turbulence viscosity.

The standard  $k - \varepsilon$  turbulence model is used to study the ferrochrome droplet behavior, referring to the industrial smelting process. The turbulence kinetic energy  $k$  and dissipation rate  $\varepsilon$  are obtained from the following transport equations:

$$\frac{\partial(\rho k)}{\partial t} + \nabla \cdot (\rho k \vec{u}) = \nabla \cdot \left[ \left( \mu_l + \frac{\mu_t}{\sigma_k} \right) \nabla k \right] + G_k - \rho \varepsilon \quad [24]$$

$$\frac{\partial(\rho \varepsilon)}{\partial t} + \nabla \cdot (\rho \varepsilon \vec{u}) = \nabla \cdot \left[ \left( \mu_l + \frac{\mu_t}{\sigma_\varepsilon} \right) \nabla \varepsilon \right] + \frac{C_{1\varepsilon}}{k} G_k - C_{2\varepsilon} \rho \frac{\varepsilon}{k} \quad [25]$$

where  $G_k$  represents the generation of turbulence kinetic energy due to the mean velocity gradients,  $C_{1\varepsilon}$  and  $C_{2\varepsilon}$  are constants ( $C_{1\varepsilon} = 1.44$ ,  $C_{2\varepsilon} = 1.92$ ),  $\sigma_k$  and  $\sigma_\varepsilon$  are the turbulent Prandtl numbers for  $k$  and  $\varepsilon$  ( $\sigma_k = 1.0$ ,  $\sigma_\varepsilon = 1.3$ ),  $\mu_t$  is the turbulent viscosity, computed as  $\mu_t = \rho C_\mu \frac{k^2}{\varepsilon}$ , and  $C_\mu$  is a constant ( $C_\mu = 0.09$ ). Standard wall functions are adopted in the present modeling.

### III. NUMERICAL SIMULATION CONFIGURATIONS

#### A. Computational Domain and Grids

The SAF is operated by constant voltage. Table II lists the main structural parameters of SAF are corresponding to Figure 3. The submerged arc is also a part of the submerged arc furnace, which is directly below the electrode. With the cycle of alternating current, it goes through arc ignition and arc extinguishing. In the figure, the representative grids are demonstrated. The grids are

Table I. Composition of All Phases

Phases	Furnace Burden	Slag	Ferrochrome
Composition	Cr <sub>2</sub> O <sub>3</sub> , iron oxides, nonmetallic oxides, furnace gas	nonmetallic oxides	Cr, Fe, C, Si, P, S

refined on the boundaries and the regions with large temperature gradients. Three sets of grids are tested to prove grid independence.

### B. Physical Properties

The physical properties are extracted from various references which are summarized in Tables III and IV.<sup>[6,30–36]</sup> The physical parameters of furnace burden change with temperature. The state of slag and ferrochrome is liquid. Table V lists the compositions of the ferrochrome.

### C. Boundary Conditions

Each simulation describes a transient smelting phenomenon in the SAF. Since this work focuses on ferrochrome settling behavior, it has high computational requirements. Therefore, the simulation results of stable smelting stage are used as the initial field, where the heat and mass transfer among the furnace burden-slag-ferrochrome phase flow are solved. Then, the resulting electric resistance, temperature, and mass

fraction are used as the initial conditions of the present model. In this way, the effects of the submerged arc are considered. Necessarily, the arc voltage drop is a part of the phase voltage in the present model, which is different from the free-burning arc.

With the pre-calculation described above, the boundary conditions of the submerged arc are determined for the current simulations. Note that the simulation results of the submerged arc are transient. Therefore, the arc voltage drops  $\bar{\varphi}_{Arc}$  of three electrodes need to be averaged. The thermal boundary conditions of arc interface  $T_{Arc,side}$  and arc bottom  $T_{Arc,bottom}$  are arithmetic means. The temperature of furnace burden upper surface  $T_{Fur,upper}$ , furnace hearth sidewall  $T_{Fur,sidewall}$ , and furnace hearth bottom  $T_{Fur,bottom}$  are obtained simultaneously. Table VI lists the boundary information of the submerged arc and furnace hearth.

It means that the electric resistance in the furnace remains unchanged when the smelting reaches the stable smelting stage. The phase voltage increases from 75 to 85 V, and the arc voltage drop increases by 15.24 pct. No slip boundary conditions are applied at walls. Table VII lists the boundaries for the electric potential, magnetic vector potential, thermal, reactant mass fraction, turbulence kinetic energy, and dissipation rate. The volume fraction of the furnace burden phase is 1 at the beginning.

The furnace burden voltage  $\varphi_m$  is loaded to the arc bottom, specified as:

$$\varphi_m = (\varphi_{Phase} - \bar{\varphi}_{Arc}) \times \sqrt{2} \times \sin(2\pi \cdot f \cdot t + \varphi) \quad [26]$$

where  $\varphi_{Phase}$  is the phase voltage,  $f$  is the AC frequency of 50 Hz,  $\varphi$  represents the three-phase alternating current where the voltage of each phase is lag off by 120 degrees, and  $n$  is the normal vector on the outer side of the furnace.  $\frac{\partial \varphi}{\partial n} = 0$  imposes that there is

**Table II. Detailed Dimensions of Structural Parameters**

Parameters	Dimension
Furnace Burden Diameter $d_1$ , mm	7910
Pitch Circle Diameter of Electrode $d_2$ , mm	3290
Electrode Diameter $d_3$ , mm	1350
Furnace Hearth Height $h_1$ , mm	3190
Electrode Insertion Depth $h_2$ , mm	1790
Arc Length $h_3$ , mm	100
Electrode Height $h_4$ , mm	4500

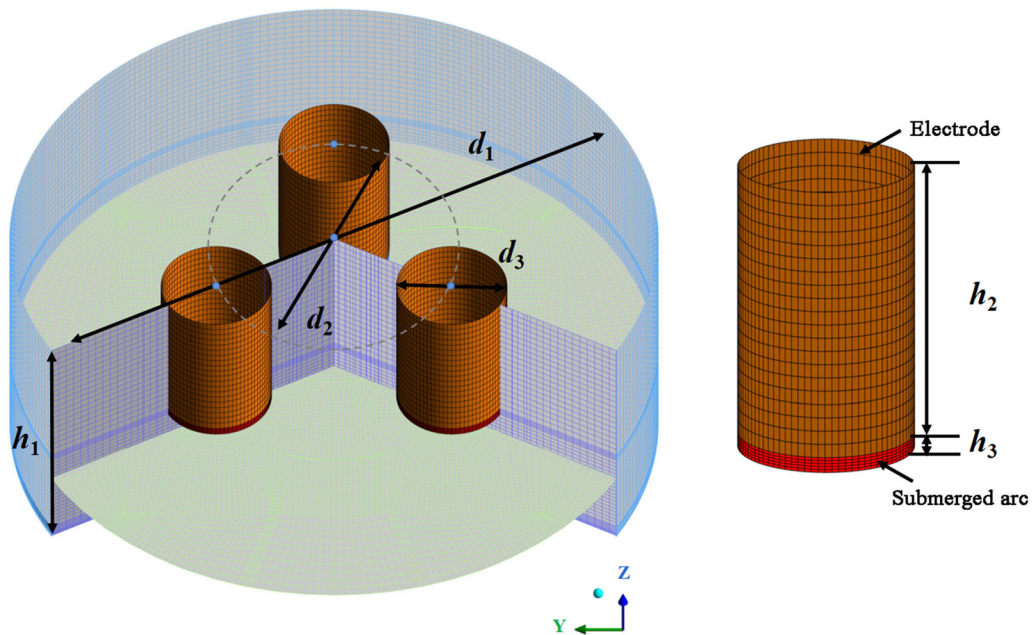


Fig. 3—Geometric and grid representation of the SAF.

**Table III. Physical Properties of Furnace Burden**

$T$ , K	673	1073	1473	1773	2073
$\rho$ , kg/m <sup>3</sup>	2600				
$c_p$ , J/(kg K)	971.3	989.0	1077.5	1107.6	1344.3
$\lambda$ , W/(m K)	$\lambda = 1 \times 10^{-6}T^2 + 0.002T + 0.41$				
$\sigma$ , S/m	0.075	0.15	15	150	150
$\mu$ , Pa s	$T < 1773$ K, $\mu = \infty$	$T = 1813$ K, $\mu = 1$	$T = 1855$ K, $\mu = 0.582$	$T = 1918$ K, $\mu = 0.408$ $T = 1960$ K, $\mu = 0.333$	$T = 2001$ K, $\mu = 0.281$ $T = 2023$ K, $\mu = 0.26$

**Table IV. Physical Properties of Slag and Ferrochrome**

Physical Properties	Slag	Ferrochrome
$\rho$ , kg/m <sup>3</sup>	2800	5691
$c_p$ , J/(kg·K)	963.0	1484.7
$\lambda$ , W/(m·K)	57.0	42.3
$\sigma$ , S/m	60.0	$9.3 \times 10^6$
$\mu$ , Pa·s	0.582	$1.576 \times 10^{-3}$
$T_{Liquidus}$ , K	1650	1850
$\mu_0$ , H/m		$4\pi \times 10^{-7}$
Furnace Burden-Ferrochrome Surface Tension, N/m		0.12
Slag-Ferrochrome Surface Tension, N/m		0.615

**Table V. Compositions of Ferrochrome**

Composition	Cr	Fe	C	Si	P	S
Percentage, pct	40–60	27–47	10	3.0	0.04	0.04

**Table VI. Boundary Information of Submerged Arc and Furnace Hearth**

Parameters	75 V	80 V	85 V
$\bar{\varphi}_{Arc}$ , V	7.38	7.66	8.50
$T_{Arc,side}$ , K	3186.32	3488.31	3494.4
$T_{Arc,bottom}$ , K	3331.89	3353.14	3508.55
$T_{Fur,upper}$ , K	1009.94	1029.61	1047.39
$T_{Fur,side}$ , K	1024.51	1049.84	1072.41
$T_{Fur,bottom}$ , K	1511.73	1549.95	1584.72

no current flowing out.  $\frac{\partial \vec{A}}{\partial n} = 0$  means that no magnetic flows out of the furnace.  $\frac{\partial c}{\partial n} = 0$  represents that the metallic oxide isn't outflow.

#### D. Numerical Procedure

Simulations are performed with the finite volume method based on the commercial software ANSYS-FLUENT. The electro-thermal conversion, heat transfer, reduction reactions, and multiphase flow are solved simultaneously by user-defined scalar equations equipped with suitable source terms. Transient simulations are carried out with a time step of 0.005 s to fulfill the convergence criteria. The pressure-velocity coupling

is realized with the widely used SIMPLE algorithm. A second-order upwind scheme is adopted to discretize the equations. The time discretization is resolved by a first order upwind scheme. The courant number is considered under 1.0 for the time discretization.

## IV. RESULTS AND DISCUSSION

The numerical predictions provide some valuable insights into the furnace production, herein a better understanding of the smelting process. The proposed model is verified first. In terms of the alternating current SAF, the electromagnetic field, temperature distribution, ferrochrome settling behavior, flow field, and productivity are discussed in detail. Furthermore, the effects of phase voltage are illustrated.

#### A. Model Validation

A grid-independence verification is carried out based on three different grid resolutions. The grid nodes are of 0.45 million, 0.6 million, and 0.75 million, named N1, N2, and N3, respectively. The SAF with the phase voltage of 75 V and the electrode insertion depth of 1.79 m is considered. The average electric current  $\bar{I}$  under different grid schemes is compared, which is listed in Table VIII. It means that the results are insensitive the grid schemes. Considering the computing resources and the proper capture of interface fluctuations, N2 grid is obtained. It is a practical trade-off between model accuracy and computational resources.

Due to the high temperature and large current during industrial production, it is difficult to obtain experimental data. Therefore, the model validation is carried out in a progressive way. First, the arc-forming stage was verified by previously.<sup>[7]</sup> Then, the temperature field was validated in the stable smelting stage. Ranganathan and Godiwalla<sup>[13]</sup> adopted the thermocouple as a probe to measure the furnace temperature except for the area around the electrode and arc. The data is considered for model validation. The predicted temperature is extracted along A-Line. The coordinates of the A-Line are from (− 3.955, 0, 2.19) to (3.955, 0, 2.19). As shown in Figure 4, the temperature predictions reasonably agree with the measurement data of Ranganathan and Godiwalla. The under predictions ( $x > 3$  mm) may be attributed to the uncertainty of the boundary conditions and simplification of the chemical reactions.

Lastly, the numerical predictions are also validated against the industrial data. The energy consumption of ferrochrome obtained from the actual smelting process is around 3100 kW·h/t at the phase voltage of 75 V. The energy consumption  $E_C$  of ferrochrome is computed as:

$$E_C = \frac{3 \times (\varphi_{Phase} + \varphi_{Ele} + \varphi_{SN}) \times \bar{I} \times t'}{m_{FC}} \quad [27]$$

where  $\varphi_{Ele}$  is the voltage of the electrode,  $\varphi_{SN}$  is the voltage of the short network,  $t'$  is 1 hour,  $m_{FC}$  is the output of the ferrochrome. According to Eq. [27], the predicted energy consumption is 3049.25 kW·h/t at the same phase voltage. The prediction error is 1.64 pct. The above results suggest that the present integrated model is satisfactorily reliable.

### B. Joule Heat Distribution

It is established that the temperature is high in a region where the value of Joule heat is large. Joule heat or arc heat is produced by electric current in the electromagnetic field. Table IX lists the average electric current at various phase voltages (*i.e.*, 75, 80, and 85 V) under the same operating conditions. As the voltage increases, the average electric current increases by 13.06 pct.

Figure 5 compares the Joule heat under different phase voltages. Here, the distributions of Joule heat are considered from B-Line (Figure 5(a)) and C-Line (Figure 5(b)). B-Line is taken from (− 0.804, 1.434, 0) to (− 0.804, 1.434, 1.3), while C-Line is from (0, 0, 0) to (0, 0, 3.19). As seen in Figure 5(a), with increasing phase voltage, the Joule heat increases less at  $z < 0.5$  m but significantly at  $z > 1.0$  m. The maximum of the Joule heat increases by 128.19 pct. Figure 5(b) shows that the Joule heat rises first and then decreases along C-Line. The Joule heat reaches the maximum for a phase voltage of 85 V at  $z = 1.18$  m, which is 1.28 times higher than that for a phase voltage of 75 V.

### C. Temperature Distribution

Temperature distribution plays a crucial role in the smelting process. Figure 6 presents such results under different phase voltages on the B-C Plane, suggesting that the temperature is nonuniform in the furnace. Electromagnetic, reduction reactions and multiphase flows collectively affect the temperature distribution. Relatively low temperature is mainly present on the top and sidewall of the furnace hearth. Near the furnace hearth bottom, the temperature is higher under the three electrodes than in the other places. As the smelting process proceeds, the overall temperature within the furnace burden gradually increases with the phase voltage, which is 1116.98, 1161.51, and 1176.63 K for the three voltages, respectively. Therefore, increasing the phase voltage is beneficial to raise the temperature. However, this has an adverse influence on the service life of the furnace lining.

Figure 7 shows the temperature distributions on three cross-sections: A-Plane ( $z = 2.19$  m), D-Plane ( $z = 1.2$  m), and E-Plane ( $z = 0.7$  m). At the same phase voltage, the temperature on the A-Plane is lower than on the other two planes. The temperature in the pitch circles of electrodes is the highest in the A-Plane. However, the temperature below the arc bottom is the highest in both D-Plane and E-Plane. This phenomenon is caused by the settling behavior of ferrochrome droplets, which takes the heat to the furnace bottom. Comparing different phase voltages on the planes at the same height suggests that the high-temperature area is the largest at a phase voltage of 85 V.

Figure 8 shows the temperature variation along C-Line at different phase voltages. The average temperature value at  $z = 0$  is 1497.94 K, 1561.65 K, and 1598.80 K for the three phase voltages. The phase voltage of 85 V results in a higher temperature than the other two phase voltages. The maximum temperature exists at 0.88 m for the phase voltage of 85 V, equaling 1710.29 K. Therefore, the phase voltage of 85 V contributes the most to the heat and mass transfer among furnace burden-slag-ferrochrome phase.

### D. Ferrochrome Settling Behavior

Within the furnace, the ferrochrome is generated by reduction reactions. Meanwhile, a certain amount of slag is also generated during the smelting process.<sup>[6]</sup> Figure 9 is the evolution of slag and ferrochrome phases with time. The reduction reactions first occur in the high-temperature region below the electrode (Figure 9(a)). After the reaction completion, the remaining nonmetallic mineral materials enter the slag droplets. The ferrochrome and slag droplets are staggered. As shown in Figures 9(b) and (c), the slag phase separates from the ferrochrome phase at the bottom of the furnace hearth. The slag layer is above the ferrochrome layer.

A closer examination of the interface characteristics helps gain more insights into the location and motion behavior of droplets. Figure 10 shows the fluctuation of the ferrochrome interface. It also includes the temperature distribution on the furnace hearth bottom. The



**Table VII. Boundary Conditions**

Boundary	$\varphi, \text{V}$	$\vec{A}, \text{V s m}^{-1}$	$T, \text{K}$	$c, \text{pct}$	$k \text{ (J)}$	$\varepsilon$
Electrode Sidewall	$\frac{\partial \varphi}{\partial n} = 0$	$\frac{\partial \vec{A}}{\partial n} = 0$	1200	$\frac{\partial c}{\partial n} = 0$	$\frac{\partial k}{\partial n} = 0$	$\frac{\partial \varepsilon}{\partial n} = 0$
Arc Side	$\frac{\partial \varphi}{\partial n} = 0$	$\frac{\partial \vec{A}}{\partial n} = 0$	$T_{Arc,side}$	$\frac{\partial c}{\partial n} = 0$	$\frac{\partial k}{\partial n} = 0$	$\frac{\partial \varepsilon}{\partial n} = 0$
Arc Bottom	$\varphi_1 = (\varphi_{Phase} - \bar{\varphi}_{Arc}) \times \sqrt{2} \times \sin(2\pi \cdot f \cdot t)$ $\varphi_2 = (\varphi_{Phase} - \bar{\varphi}_{Arc}) \times \sqrt{2} \times \sin(2\pi \cdot f \cdot t + \frac{2\pi}{3})$ $\varphi_3 = (\varphi_{Phase} - \bar{\varphi}_{Arc}) \times \sqrt{2} \times \sin(2\pi \cdot f \cdot t + \frac{4\pi}{3})$	$\frac{\partial \vec{A}}{\partial n} = 0$	$T_{Arc,bottom}$	$\frac{\partial c}{\partial n} = 0$	$\frac{\partial k}{\partial n} = 0$	$\frac{\partial \varepsilon}{\partial n} = 0$
Burden Upper Surface	$\frac{\partial \varphi}{\partial n} = 0$	$\frac{\partial \vec{A}}{\partial n} = 0$	$-\lambda \cdot \frac{\partial T}{\partial n} = 2 \times (T - T_{Fur,upper})$	$\frac{\partial c}{\partial n} = 0$	$\frac{\partial k}{\partial n} = 0$	$\frac{\partial \varepsilon}{\partial n} = 0$
Hearth Sidewall	$\frac{\partial \varphi}{\partial n} = 0$	$\vec{A} = 0$	$-\lambda \cdot \frac{\partial T}{\partial n} = 10 \times (T - T_{Fur,sidewall})$	$\frac{\partial c}{\partial n} = 0$	$\frac{\partial k}{\partial n} = 0$	$\frac{\partial \varepsilon}{\partial n} = 0$
Hearth Bottom	$\varphi = 0$	$\frac{\partial \vec{A}}{\partial n} = 0$	$-\lambda \cdot \frac{\partial T}{\partial n} = 2 \times (T - T_{Fur,bottom})$	$\frac{\partial c}{\partial n} = 0$	$\frac{\partial k}{\partial n} = 0$	$\frac{\partial \varepsilon}{\partial n} = 0$

**Table VIII. Comparison of Electric Current Under Three Different Grids**

Grid Nodes	N1 Grid	N2 Grid	N3 Grid
$\bar{I}, \text{kA}$	75.55	79.08	77.66

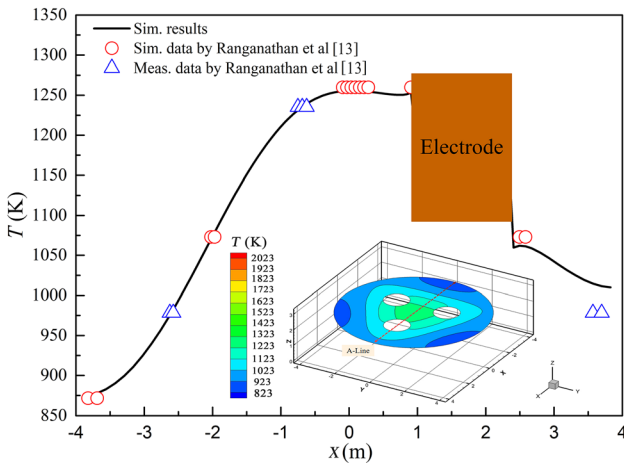


Fig. 4—Comparison of measured and predicted temperature.

**Table IX. Average Electric Current Under Different Phase Voltage**

$\varphi_{Phase}, \text{V}$	75	80	85
$\bar{I}, \text{kA}$	79.08	84.55	89.41

ferrochrome settling behavior is demonstrated under different phase voltages. The height of falling ferrochrome ranges from 0 to 1.3 m along the  $z$  axis. As seen in Figure 10, the ferrochrome generation concentrates both under and around the submerged arc. With increasing phase voltage, the amount of ferrochrome rises gradually. The ferrochrome drops to the furnace

bottom, through which the heat is taken downward. Overall, the temperature at the pitch circle of the electrodes is higher than in the other regions. Comparing with the temperature distributions suggest that the settling path of ferrochrome droplets appears within the high-temperature area (Figure 6).

Once the temperature is high enough, reduction reactions start. The reactions yield the desired ferrochrome and simultaneously produce slag. The ferrochrome presents in the form of droplets, which settle through the furnace burden. As shown in Figures 10 and 11, the motion of ferrochrome droplets at the interface can be characterized into two types. One exhibits violently falling droplets, resulting in the mass transfer from the furnace burden phase to the ferrochrome phase. The other is the calm plane of the ferrochrome phase at the furnace hearth bottom. The location of ferrochrome droplets can be determined. As the phase voltage increases, the ferrochrome generation starts from the arc bottom to the pitch circle of the electrode. With the development of smelting time, three calm planes converge into a large plane.

Figure 12 shows the velocity vectors under various phase voltages. Note that the flows could have a profound effect on the smelting state. The flows of furnace burden, slag and ferrochrome phases are driven by Lorentz force, surface tension, and gravitational force. The flow direction of the furnace burden is downward near the electrode. The maximum velocity is mainly under the electrode, which is related to the ferrochrome settling behavior. With increasing phase voltage, the velocity magnitude gradually increases. The maximum velocity reaches up to 0.057 m/s for the phase voltage of 85 V, resulting from the ferrochrome settling behavior.

### E. Ferrochrome Productivity

Ferrochrome production mainly depends on reduction reactions. The factors affecting the reactions include reaction condition, conversion rate and reactant mass fraction. The key reaction condition is that the

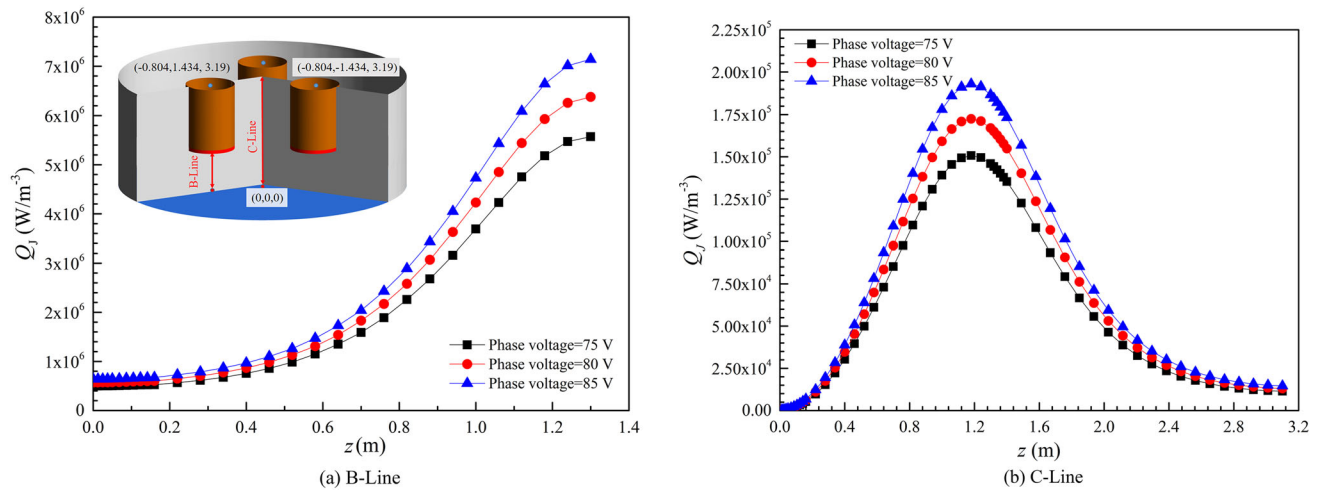


Fig. 5—Comparison of Joule heat under different phase voltages: (a) B-Line. (b) C-Line.

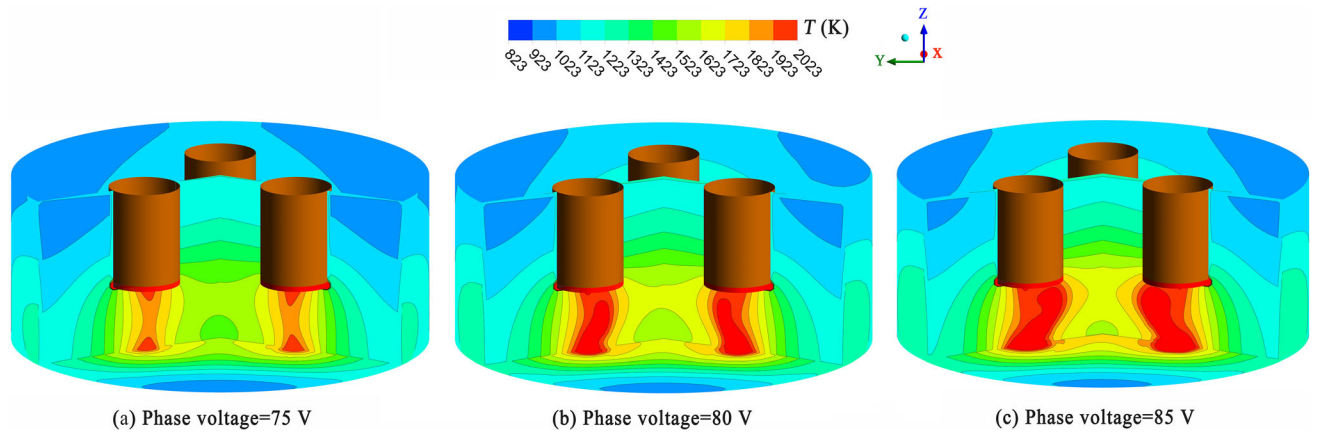


Fig. 6—Temperature distributions under different phase voltages: (a) Phase voltage = 75 V. (b) Phase voltage = 80 V. (c) Phase voltage = 85 V.

temperature reaches the reaction initial temperature while the reactant mass fraction is larger than 0. Figure 13 is the variation of the  $\text{Cr}_2\text{O}_3$  mass fraction distribution along B-Line. According to the distribution of  $\text{Cr}_2\text{O}_3$ , the reaction area changes little at the center of furnace. There are no reactions near the furnace hearth sidewall and the upper furnace burden because of the low temperature. However, the reduction proceeds significantly under the electrode bottom due to the high conversion rate of  $\text{Cr}_2\text{O}_3$ . The variation of phase voltage greatly influences the mass fraction of  $\text{Cr}_2\text{O}_3$  along B-Line. The reaction is more complete when the phase voltage is 85 V. At this phase voltage, the ferrochrome phase exists on the furnace hearth bottom. With increasing phase voltage, the mass fraction of  $\text{Cr}_2\text{O}_3$  decreases.

Figure 14 presents the variation of iron oxide mass fraction with phase voltage. It can be observed that reactions occur significantly in the furnace. The reduction reactions are inactive at the vicinity of the furnace hearth sidewall. The phase voltage has a little influence on the mass fraction of iron oxides. According to the

mass fraction of iron oxides along C-Line, the reaction is more active with the increase of phase voltage above the electrode insertion depth ( $z = 1.79$  m). The phenomenon is opposite under the electrode insertion depth.

The mass transfer between the furnace burden and the slag and ferrochrome production is highly important to SAF performance. It is established that the content of iron and chromium in ferrochrome significantly impacts the smelting process. In the initial state, the total mass contained within the furnace is 243.12 tons. By integrating the ferrochrome elements in the furnace inner space, ferrochrome output is calculated. It is 5.91, 5.86, 6.86 t/h for the three phase voltages (Figure 15). With the increase of phase voltage, the ratio of chromium to iron changes from 33.22, 56.54, to 70.47 pct. For the phase voltage of 85 V, the ferrochrome productivity is higher than the other two phase voltages. Correspondingly, the energy consumption of ferrochrome is also different. The energy consumption values are 3049.25, 3512.17, and 3363.81 kW·h/t. When the phase voltage is 80 V, the energy consumption of the ferrochrome is the

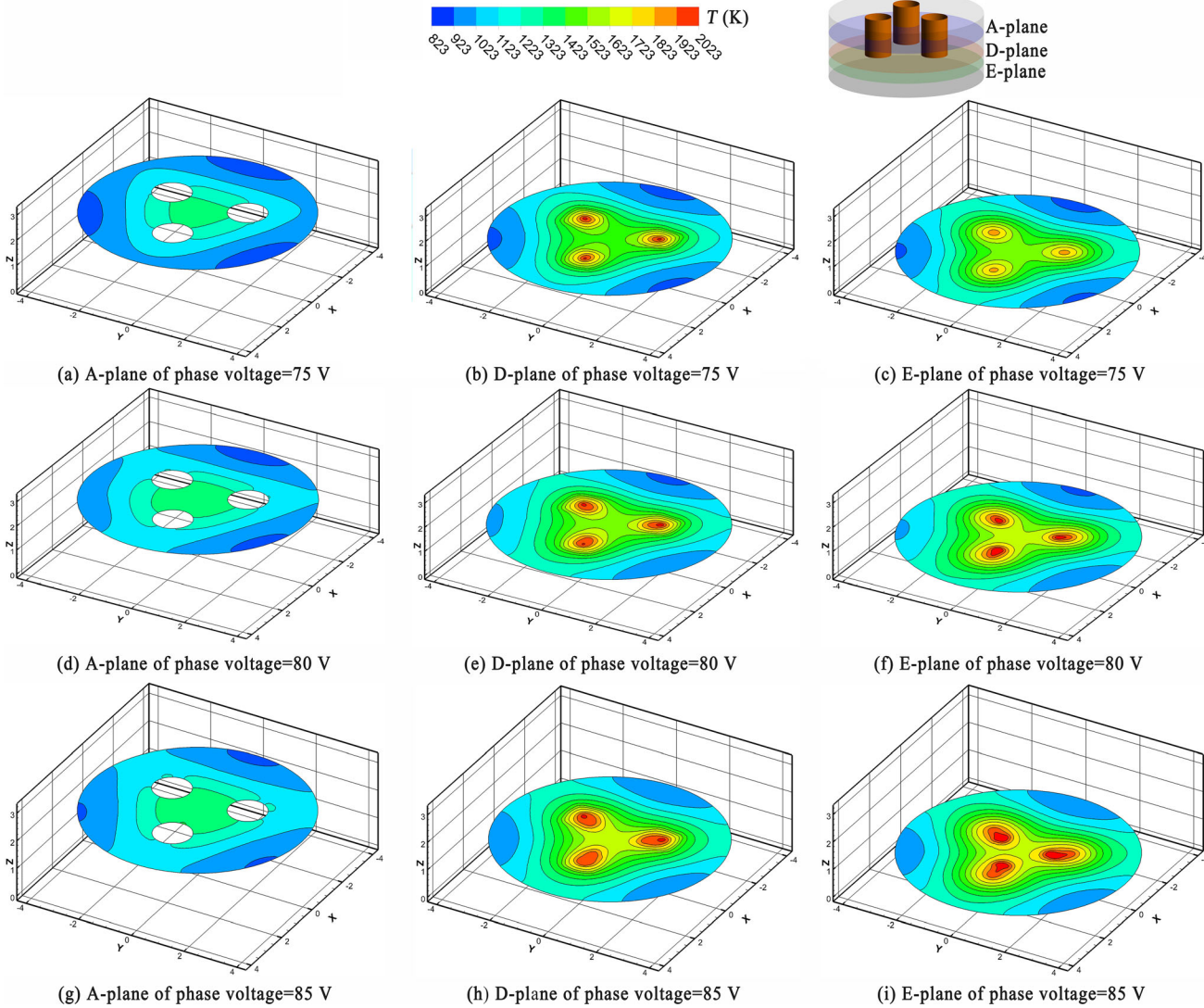


Fig. 7—Temperature contours on representative cross-sections at different heights: (a) A-plane of phase voltage = 75 V. (b) D-plane of phase voltage = 75 V. (c) E-plane of phase voltage = 75 V. (d) A-plane of phase voltage = 80 V. (e) D-plane of phase voltage = 80 V. (f) E-plane of phase voltage = 80 V. (g) A-plane of phase voltage = 85 V. (h) D-plane of phase voltage = 85 V. (i) E-plane of phase voltage = 85 V.

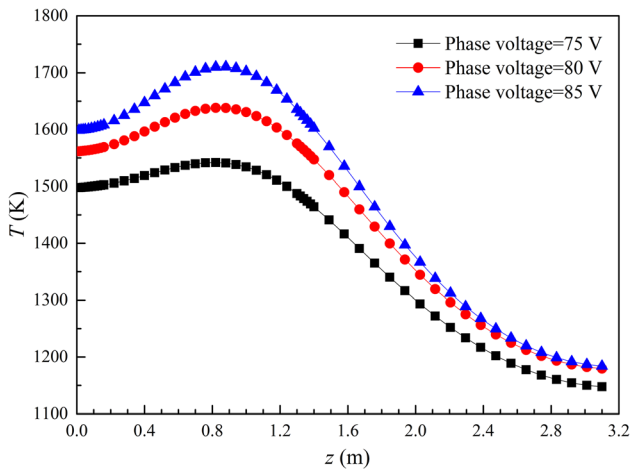


Fig. 8—Comparison of temperature along C-Line at different phase voltages.

highest. However, the output of ferrochrome is only 0.96 pct less than that of 75 V. Thus, it can be concluded that the increase of voltage is beneficial to the increase of chromium content in ferrochrome.

## V. CONCLUSION

A 3D transient mathematic model is developed to study the smelting phenomena and ferrochrome productivity in the alternating current submerged arc furnace. In the model, the electro-thermal conversion, heat transfer, ferrochrome generation and multiphase flow are solved simultaneously. The predicted results are in good agreement with the measured energy consumption of industrial production. The findings are useful to guide the actual production, although some assumptions exist in the numerical simulation, as summarized below:

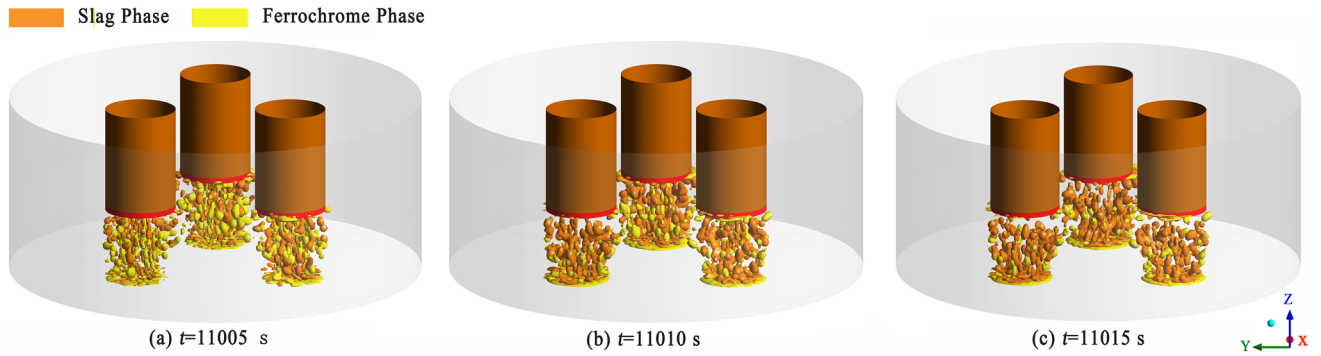


Fig. 9—Evolution of slag and ferrochrome phases with time (Phase voltage = 75 V): (a)  $t = 11,005$  s. (b)  $t = 11,010$  s. (c)  $t = 11,015$  s.

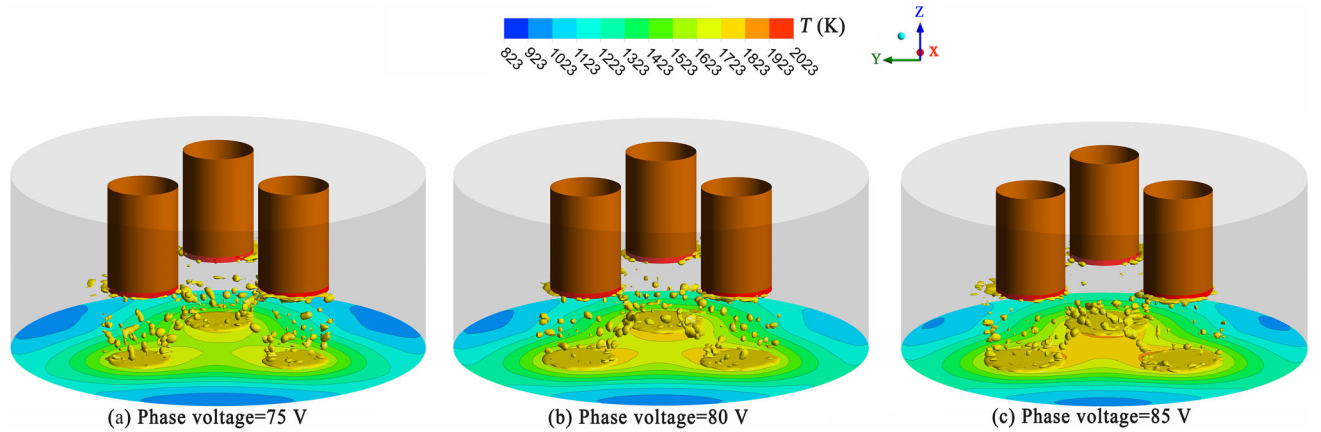


Fig. 10—Ferrochrome settling behavior during the smelting process: (a) Phase voltage = 75 V. (b) Phase voltage = 80 V. (c) Phase voltage = 85 V.

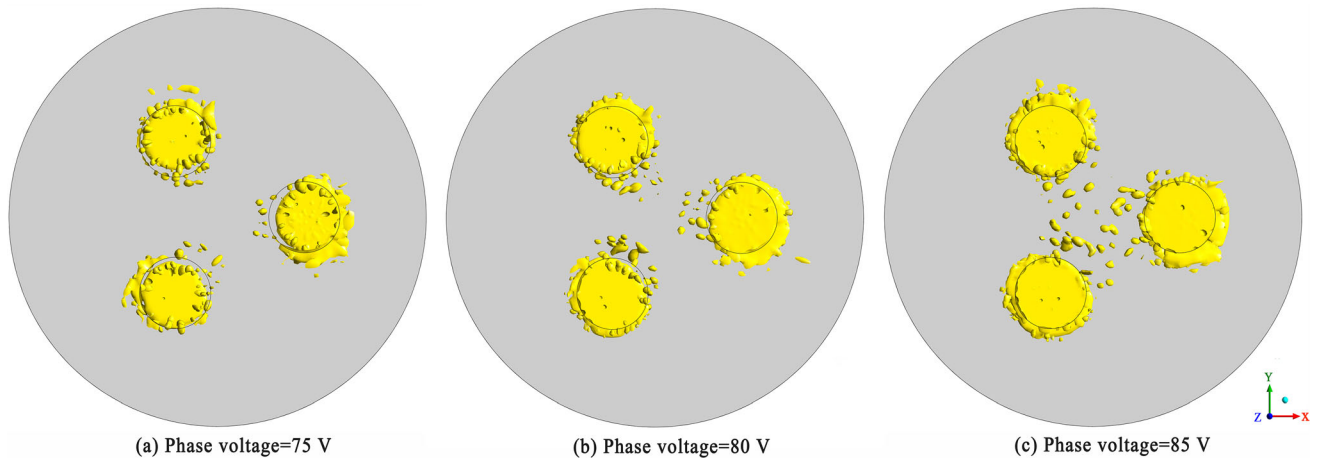


Fig. 11—Locations of ferrochrome droplets under different phase voltages: (a) Phase voltage = 75 V. (b) Phase voltage = 80 V. (c) Phase voltage = 85 V.

- 1) As the phase voltage increases from 75 to 85 V, the average arc voltage drop increases by 15.24 pct. At the same time, the average current increases by 13.06 pct. The melting area with a phase voltage of 85 V is the largest. The maximum velocity reaches up to 0.057 m/s for a phase voltage of 85 V, which is a result of the ferrochrome settling behavior.
- 2) Most ferrochrome droplets are generated under the submerged arc. Overall, the behavior of ferrochrome droplets has a significant impact on the smelting process. The interfaces among the furnace burden-slag-ferrochrome phases exhibit two distinguishing behaviors. The violently falling droplets



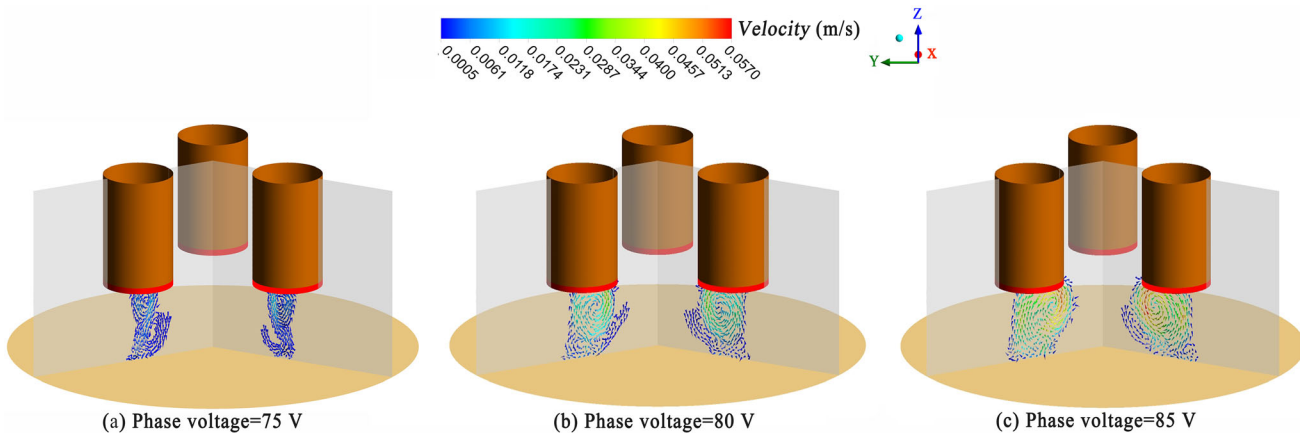


Fig. 12—Velocity vector distributions under different phase voltages: (a) Phase voltage = 75 V. (b) Phase voltage = 80 V. (c) Phase voltage = 85 V.

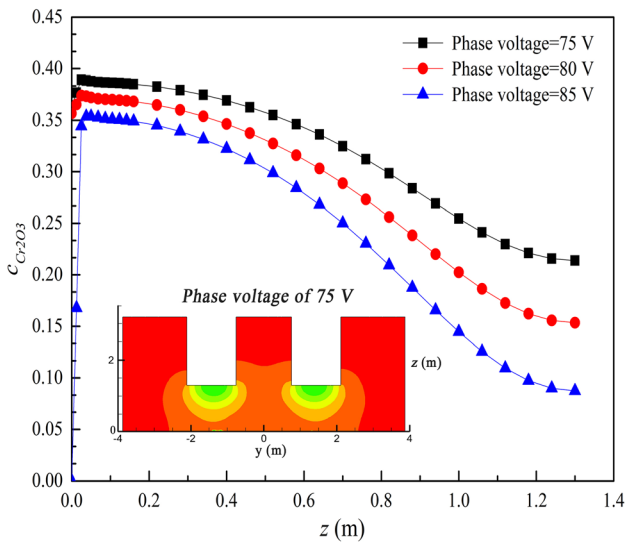


Fig. 13—Mass fraction distributions of  $\text{Cr}_2\text{O}_3$  under different phase voltages.

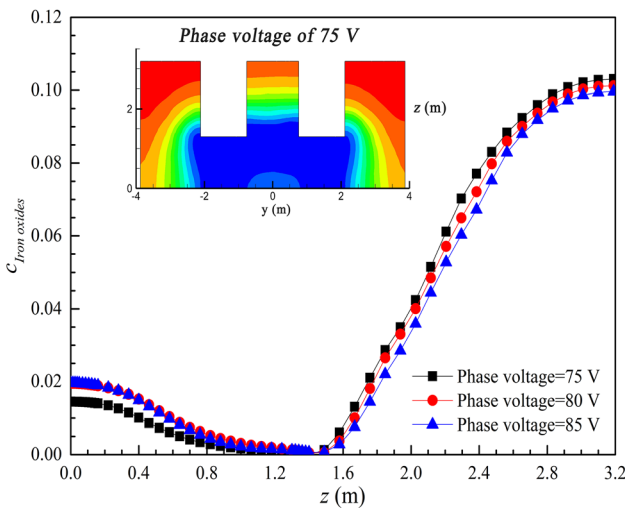


Fig. 14—Mass fraction distributions of iron oxides under different phase voltages.

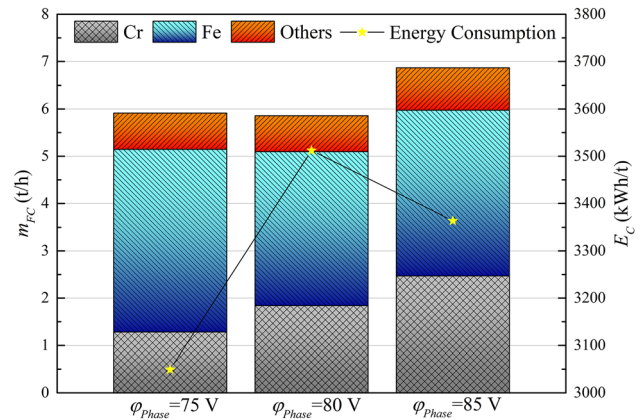


Fig. 15—Ferrochrome outputs and energy consumption under different phase voltages.

characterize one and the other is described as droplets collection into the calm plane.

- 3) No reactions occur near the furnace hearth sidewall and the upper furnace burden because of the low temperature. However, the mass fraction of  $\text{Cr}_2\text{O}_3$  reduces more obviously under the arc bottom due to the high temperature. Most iron oxides are consumed *via* reduction reactions under the current process condition.
- 4) Increasing the phase voltage has an advantage in terms of chromium content in ferrochrome. Energy consumption depends not only on the output of products but also on the content of ferrochrome elements. When the phase voltage is 85 V, the energy consumption is low, and the ferrochrome quality is high.

## ACKNOWLEDGMENTS

This work was supported by the National Natural Science Foundation of China (Nos. 51934002 and 52171031), Research and Evaluation Facilities for Ser-

vice Safety of Major Engineering Materials National Major Science and Technology Infrastructure Open Project Fund (MSAF-2021-009), and the 111 Project (B16009).

### CONFLICT OF INTEREST

On behalf of all authors, the corresponding author states that there is no conflict of interest.

### NOMENCLATURE

$a$	Absorption coefficient
$A$	Pre-exponential term, $s^{-1}$
$\vec{A}$	Magnetic potential vector, $V\ s\ m^{-1}$
$b$	Serial number of different grid
$\vec{B}$	Magnetic field, T
$c$	Reactant mass fraction
$\Delta c$	Variation of reactant mass fraction
$c_p$	Heat capacity, $J/(kg\cdot K)$
$e$	Electronic charge, $-1.6 \times 10^{-19}\ C$
$E_a$	Activation energy, $kJ/mol$
$E_C$	Energy consumption, $kWh/t$
$\vec{F}_L$	Lorentz force, $N/m^3$
$\vec{F}_{st}$	Surface tension, $N/m^3$
$g$	Gravity, $m/s^2$
$G_k$	Generation of turbulence kinetic energy
$h$	Heat transfer coefficient, $W/(m^2\cdot K)$
$i$	Serial number of different phase
$I$	Radiation intensity which depends on position ( $\vec{r}$ ) and direction ( $\vec{s}$ )
$\bar{I}$	Average electric current, A
$j$	Serial number of simplified reaction
$\vec{J}$	Electric current density, $A/m^2$
$k$	Turbulence kinetic energy, J
$K$	Reaction rate constant, $s^{-1}$
$K_B$	Boltzmann's constant, $0.025852\ eV$
$M$	Reactant amount, mol
$M_P$	Molar mass of product, $kg/mol$
$M_R$	Molar mass of reactant, $kg/mol$
$m$	Total number of phases
$m_{FC}$	Output of ferrochrome, $t/h$
$n$	$x$ , $y$ And $z$ axial direction
$n'$	Refractive index
$N$	Coefficient to determine whether the reaction occurs
$P$	Pressure, Pa
$p$	The mass ratio of slag to ferrochrome
$q$	Heat absorbed by reactions, $J/mol$
$Q_{Arc}$	Arc heat, $W/m^3$
$Q_J$	Joule heat of multiphase, $W/m^3$
$Q_{Rea}$	Reaction heat, $W/m^3$
$\vec{r}$	Path length
$R$	Ideal gas constant, $8.314\ J/(mol\cdot K)$
$R_{SN}$	Short network electric resistance, $m\Omega$
$s$	Direction vector
$\vec{s}$	Direction vector
$\vec{s}'$	Scattering direction vector
$S_C$	Variation of reactant, $kg/(m^3\cdot s)$

$S_{i,j}$	Mass transfer rate, $kg/(m^3\ s)$
$T$	Temperature, K
$t$	Physical time, s
$\Delta t$	Simulation time step, s
$t'$	One hour, h
$\vec{u}$	Velocity of mixture phase, $m/s$
$\vec{v}$	Virtual vertical downward-velocity of the packed bed, $s^{-1}$
$X$	Mass fractional conversion rate of reaction, $s^{-1}$
$X_{Fe}$	Mass fractional conversion rate of iron reduction, $s^{-1}$
$X_{Cr}$	Mass fractional conversion rate of chromium reduction, $s^{-1}$

### GREEK SYMBOLS

$\alpha$	Phase volume fraction
$\delta$	Stefan–Boltzmann constant, $5.669 \times 10^{-8}\ W/(m^2\cdot K^4)$
$\varepsilon$	Turbulence dissipation rate
$\mu$	Viscosity, Pa·s
$\mu_0$	Magnetic conductivity, H/m
$\mu_l$	Laminar viscosity, Pa·s
$\mu_t$	Turbulence viscosity, Pa·s
$\lambda$	Thermal conductivity, $W/(m\cdot K)$
$\mu_{eff}$	Effective viscosity composed of the turbulence viscosity, Pa·s
$\rho$	Fluid density, $kg/m^3$
$\sigma$	Electrical conductivity, S/m
$\sigma_k$	Turbulent Prandtl numbers for $k$
$\sigma_\varepsilon$	Turbulent Prandtl numbers for $\varepsilon$
$\sigma_s$	Scattering coefficient
$\varphi$	Electric potential, V
$\cos\varphi$	Power factor
$\gamma$	Relative deviation ratio
$\Phi$	Phase function
$\Omega'$	Solid angle
$(a + \sigma_s)s$	Optical thickness or opacity of the medium

### REFERENCES

- Z. Chen, W. Ma, K. Wei, J. Wu, S. Li, K. Xie, and G. Lv: *Appl. Therm. Eng.*, 2017, vol. 112, pp. 226–36.
- R.T. Jones and M.W. Erwee: *Calphad*, 2016, vol. 55, pp. 20–25.
- Y. Yu, B. Li, C. Wang, Z. Fang, X. Yang, and F. Tsukihashi: *Energy*, 2019, vol. 179, pp. 792–804.
- P. Liu, B. Li, S.C.P. Cheung, and W. Wu: *Appl. Therm. Eng.*, 2016, vol. 109, pp. 542–59.
- B. Friedrich, M. Kalisch, D. Friedmann, R. Degel, F. Kaußen, and J. Bohlke: *J. Sustain. Metall.*, 2018, vol. 4, pp. 77–94.
- Y. Yu, B. Li, S. Liu, F. Qi, and Z. Liu: *INFACON XVI*, Trondheim, Norway, 2021, pp. 1–9.
- Y. Yu, B. Li, C. Yun, F. Qi, and Z. Liu: *Metall. Mater. Trans. B*, 2021, vol. 52B, pp. 3907–19.
- H.L. Larsen, G. Liping, and J.A. Bakken: *INFACON VII*, Trondheim, Norway, 1995, pp. 517–27.
- I.J. Barker, M.S. Rennie, C.J. Hockaday, P. J. Brereton-Stiles: *IFAPA XI*, 2007, pp. 685–94.
- X. Zhang, Z. Tong, D. Li, X. Hu, and Y. He: *Appl. Therm. Eng.*, 2021, vol. 185, p. 115980.

11. M. Sparta, D. Varagnolo, K. Straaboe, S.A. Halvorsen, E.V. Herland, and H. Martens: *Metall. Mater. Trans. B*, 2021, vol. 52B, pp. 1267–78.
12. G.A. Saevarsdottir, J.A. Bakken: *The twelfth International Ferrochromes Congress*, Helsinki, Finland, June 6–9 2010, pp. 717–28.
13. S. Ranganathan and K.M. Godiwalla: *Ironmak. Steelmak*, 2001, vol. 28, pp. 273–78.
14. S. Ranganathan and K.M. Godiwalla: *Can. Metall. Q.*, 2011, vol. 50, pp. 37–44.
15. Y.A. Tesfahunegn, T. Magnusson, M. Tangstad, G. Saevarsdottir: Springer International Publishing AG, 2018, pp. 518–27.
16. Y.A. Tesfahunegn, T. Magnusson, M. Tangstad, and G. Saevarsdottir: *Metall. Mater. Trans. B*, 2020, vol. 51B, pp. 510–18.
17. E. Sridhar and A.K. Lahiri: *Steel Res.*, 1994, vol. 65, pp. 433–37.
18. Y.Y. Sheng, G.A. Irons, and D.G. Tisdale: *Metall. Mater. Trans. B*, 1998, vol. 29B, pp. 85–94.
19. Y. Yang, Y. Xiao, M.A. Reuter: *International ferrochrome Congress 1–4 February 2004*, Cape Town, South Africa, pp. 15–25.
20. P.D. Barba, F. Dughiero, M. Dusi, M. Forzan, M.E. Mognaschi, M. Paioli, and E. Sieni: *Int. J. Appl. Electrom.*, 2012, vol. 39, pp. 555–61.
21. B. Andresen, J.K. Tuset: INFACON 7, Norway, 1995, pp. 517–27.
22. E. Scheepers, A.T. Adema, Y. Yang, and M.A. Reuter: *Miner. Eng.*, 2006, vol. 19, pp. 1115–25.
23. E. Scheepers, Y. Yang, A.T. Adema, R. Boom, and M.A. Reuter: *Metall. Mater. Trans. B*, 2010, vol. 41B, pp. 990–1005.
24. Z. Wang, N. Wang, T. Li: Material Science Forum, 2011, pp. 675–77, 995–98.
25. K.T. Karalis, N. Karkalos, N. Cheimarios, G.S.E. Antipas, A. Xenidis, and A.G. Boudouvis: *Appl. Math. Model.*, 2016, vol. 40, pp. 9052–66.
26. J.J. Bezuidenhout, J.J. Eksteen, and S.M. Bradshaw: *Miner. Eng.*, 2009, vol. 22, pp. 995–1006.
27. M. Kakhodabeigi, H. Tveit, and J.S. Johansen: *Trans. Iron Steel Ins. Jpn.*, 2011, vol. 51, pp. 193–202.
28. J.L. Xia, T. Kankaanp, and T. Ahokainen: *Metall. Mater. Trans. B*, 2004, vol. 35B, pp. 839–45.
29. T. Meier, K. Gandt, T. Hay, and T. Echterhof: *Steel Res. Int.*, 2018, vol. 89, pp. 1–14.
30. Y. Yu, B. Li, Z. Fang, and C. Wang: *J. Clean. Prod.*, 2021, vol. 285, p. 124893.
31. M. Dhainaut: *Tenth International Ferrochromes Congress 1–4 February 2004*, Cape Town, South Africa, pp. 605–13.
32. P. Niemelä, M. Kauppi: INFACON XI, 2007.
33. H. Kobatake and B. Jürgen: *J. Mater. Sci.*, 2013, vol. 48, pp. 6818–24.
34. R.W. Powell, R.P. Tye, and M.J. Woodman: *Philos. Mag.*, 1961, vol. 6, pp. 857–62.
35. X. Huang, B. Li, and Z. Liu: *Int. J. Heat Mass Transf.*, 2018, vol. 120, pp. 458–70.
36. M. Sun, B. Li, and L. Li: *Ind. Eng. Chem. Res.*, 2019, vol. 58, pp. 3407–19.

**Publisher's Note** Springer Nature remains neutral with regard to jurisdictional claims in published maps and institutional affiliations.

Springer Nature or its licensor (e.g. a society or other partner) holds exclusive rights to this article under a publishing agreement with the author(s) or other rightsholder(s); author self-archiving of the accepted manuscript version of this article is solely governed by the terms of such publishing agreement and applicable law.